ARTICLE

# Effect of Surface Charge on the Cellular Uptake and Cytotoxicity of Fluorescent Labeled Cellulose Nanocrystals

**Khaled A. Mahmoud, Jimmy A. Mena, Keith B. Male, Sabahudin Hrapovic, Amine Kamen, and John H.T. Luong***

Biotechnology Research Institute, Canada National Research Council, 6100 Royalmount Avenue, Montreal, Canada H4P 2R2

**ABSTRACT** Probing of cellular uptake and cytotoxicity was conducted for two fluorescent cellulose nanocrystals (CNCs): CNC-fluorescein isothiocyanate (FITC) and newly synthesized CNC-rhodamine B isothiocyanate (RBITC). The positively charged CNC-RBITC was uptaken by human embryonic kidney 293 (HEK 293) and *Spodoptera frugiperda* (*Sf*9) cells without affecting the cell membrane integrity. The cell viability assay and cell-based impedance spectroscopy revealed no noticeably cytotoxic effect of the CNC-RBITC conjugate. However, no significant internalization of negatively charged CNC-FITC was observed at physiological pH. Indeed, the effector cells were surrounded by CNC-FITC, leading to eventual cell rupture. As the surface charge of CNC played an important role in cellular uptake and cytotoxicity, facile surface functionalization together with observed noncytotoxicity rendered modified CNC as a promising candidate for bioimaging and drug delivery systems.

**KEYWORDS:** cellulose nanocrystal • fluorescence • rhodamine B isothiocyanate • fluorescein isothiocyanate • cytotoxicity • cell imaging • drug delivery

## INTRODUCTION

Highly crystalline cellulose nanocrystal (CNC) has emerged as a novel material for a plethora of important applications such as nanofillers, nanocomposites (1), surface coatings, regenerative medicine (2),and drug delivery (3). With high purity and surface area, biocompatible CNC with exceptional mechanical properties is amenable to chemical modification. In brief, the terminal OH groups on the glucose-based CNC provide facile surface modification (4), i.e., CNC can be easily functionalized or bioconjugated, resulting in a rich source of new materials and platforms for diversified bioapplications including enzyme immobilizations (5).

For effective therapy, drugs and biomarkers are designed to passively penetrate the cell membrane or to trigger active transportation (6). Large hydrophilic biomolecules such as nucleic acids and proteins cannot cross the cell membrane; nevertheless, their internalization is controlled by endocytosis (6). To date, mesoporous silica nanorods (7−9), metallic nanoparticles (10−13), carbon nanotubes (14), and polymeric micelles (15−18) are biofunctionalized for effective drug encapsulation, cellular internalization, and controlled drug release. However, such nanomaterials, including carbon nanotubes, induce cytotoxicity due to metal impurities, particle aggregation, and their long-term instability as well as decomposition inside the cell. CNC has a rod shape with sizes in the range of 200−300 nm long and 5−50 nm wide (19). This size range would allow for a prolonged circulation of CNC in the bloodstream and sufficiently delays its clearance by the mononuclear phagocytic-system (3, 20). With its anticipated production and application at large scale, bioeffects and safety of CNC to the environment and human health must be thoroughly investigated in vitro before they can be used in vivo. As an example, chitosan nanoparticles are prepared from natural food sources; nevertheless, these materials display unexpected antimicrobial activities because of their high surface area and charged effect (21).

This study describes the synthesis of two fluorescent cellulose nanocrystals (CNCs), CNC-rhodamine B isothiocyanate (RBITC) and CNC-fluorescein isothiocyanate (FITC), and investigates their ability to penetrate the membrane of two different cell lines. Covalent conjugation, as opposed to physical encapsulation, obviates the possibility of fluorophores being leached out from the nanoparticles in physiological milieu. The cytotoxicity and/or inhibitory effects of CNC are also evaluated by cell-based impedance spectroscopy and cell viability tests. Electric cell-substrate impedance sensing (ECIS) has been proven as a predictor of cytotoxicity to represent the overall cell response resulting from a variety of inhibition mechanisms (22−26).

## EXPERIMENTAL SECTION

**Materials.** Rhodamine B isothiocyanate (RBITC), fluorescein isothiocyanate (FITC), 3-(4,5-dimethylthiazol-2-yl)−2,5-diphenyl tetrazolium bromide (MTT), trypan blue, and other reagents were obtained from Sigma-Aldrich. Deionized water (18.2 MΩ cm) was obtained from Millipore Direct-Q5. HEK-293 cell line derived from human embryonic kidney cells and *Sf*9 insect cell line derived from the pupal ovarian tissue of *Spodoptera fru-*

* Corresponding author. E-mail: John.Luong@cnrc-nrc.gc.ca. Fax: (514) 496-6265.

Received for review July 16, 2010 and accepted September 17, 2010

DOI: 10.1021/am1006222





Published on Web 10/04/2010

**Scheme 1. Schematic Illustration for the Synthesis of the CNC-RBITC Conjugate: (i) Epichlorohydrin, NaOH, 60 °C; (ii) $NH_4OH$, NaOH pH 12; (iii) RBITC or FITC, Sodium Borate, Sodium Chloride, Ethylene Glycol, Tartaric Acid, and Sucrose**

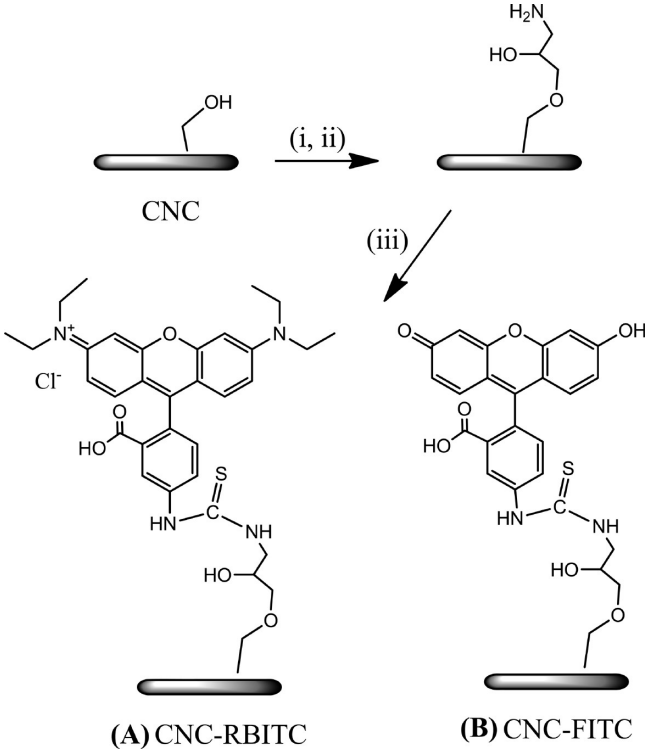


*giperda* were chosen to assess the CNC-RBITC cellular localization in mammalian and nonmammalian cells. F-17 and SF-900II media (Invitrogen, Carlsbad, CA, USA) were used for HEK-293 and *Sf*9 cell maintenance in suspension cultures, respectively. To avoid bacterial or fungal contamination, we added HyQ antibiotic/antimycotic 100X solution (Thermo Scientific, Logan, UT, USA) to the cell culture before addition of the CNC-labeled material. Plates for cell uptake studies were obtained from Corning (Corning, NY, USA).

**Preparation of Cellulose Nanocrystals (CNC).** The CNC suspension was prepared from enzyme treated flax fibers according to a previously described procedure (5). In brief, pectate lyase treated flax fibers were ground through a 20-mesh screen down to 0.85 mm fiber size. The resulting flax fibers (0.5 g) were stirred in 20 mL of an acid mixture (65% $H_2SO_4$:65% $HNO_3$ at 3:1 v/v) and 10 mL of $H_2O_2$ was added dropwise (**CAUTION:** *sulfuric acid reacts with $H_2O_2$ to release heat, and thus the reaction should be handled in the fume hood with precaution and proper safety protection*). The reaction was carried out at 45 °C for 3 h. After a 10-fold dilution with deionized water to terminate the reaction, the suspension was centrifuged at 10 000 rpm, followed by extensive washing until the resulting pH was ~6. The sample was then dialyzed against deionized water for 3 days (Spectra/Por 4 dialysis tubing 12−14 kDa). The mixed bed ion-exchange resin (Dowex MR −3) was added to the CNC suspension and allowed to stand for 2 days and was removed by filtration (Whatman 541). The colloidal solution was concentrated to ~15 mg/mL and sonicated for 35 min at room temperature. The CNC solution was lyophilized to produce white flakes.

**Synthesis and Purification of the CNC-FITC and CNC-RBITC Conjugates.** The synthetic route for these fluorescent CNCs is described in Scheme 1, following literature procedures (27−29) with minor modifications. CNC (100 mg) was reacted with epichlorohydrin (6 mmol/g CNC) in 1 M NaOH for 2 h at 60 °C to introduce the epoxy groups on the OH groups of CNCs. The reaction mixture was dialyzed (Spectra/Por 4 dialysis tubing 12−14 kDa) against deionized water to remove the unreacted reagents. The reaction mixture was then heated with 50% (w/v) NaOH, 29.4%, $NH_4OH$, pH 12 (5 mL/g CNC) for 2 h at 60 °C, followed by dialysis until the pH reached 7. RBITC or FITC (0.32 mmol/g CNC) was reacted with the primary amine groups on CNC in 50 mM sodium borate buffer solution, containing 5 mM ethylene glycol tetraacetic acid, 50 mL/g CNC, 0.15 M NaCl, and 0.3 M sucrose. The reaction mixture was stirred overnight in the dark followed by dialysis until no noticeable free dye was detected by fluorescence and UV/vis spectroscopy in the bulk water. The suspension was sonicated for 10 min in an ice bath, and filtered through a syringe filter (0.45 $\mu$m) to remove any aggregates. The final pH of the suspension (0.8 wt %) was 6.8.

**Cellular Uptake of Fluorescently Labeled Cellulose Nanocrystals.** HEK-293 cells were cultivated at 37 °C in a $CO_2$ controlled environment incubator in 12-well plates. *Sf*9 cells were cultivated at 27 °C in 12-well plates. Sterile circular coverslips (15 mm diameter) were placed inside each well prior to cell addition. HEK 293 or *Sf*9 cells (1 mL, 1 × $10^6$ cells/mL) were added to each well followed by the addition of 10 $\mu$L HyQ antibiotic/antimycotic 100X solution. Thereafter, 100 $\mu$L of CNC-RBITC (1 mg/mL) was added per well. The 12-well plates were incubated overnight under their respective conditions. The cells were then washed with 1 mL of PBS, fixed with 4% paraformaldehyde in PBS for 15 min, washed twice with PBS, and analyzed by confocal microscopy. For pH study, the growth medium pH was adjusted either with HCl or NaOH. Cells were incubated with CNC-FITC or CNC-RBITC for 8 h at the respective pH, and then fixed for confocal microscope analysis.

**Spectroscopy and Imaging.** Fourier transform infrared (FTIR) spectra were collected from 4000 to 400 $cm^{-1}$ for 64 scans at a resolution of 4 $cm^{-1}$ using a Bruker Tensor 27 FTIR spectrophotometer with samples run as KBr pellets. Fluorescence measurement was performed in 400 $\mu$L cuvettes using a Spex-Fluorolog spectrofluorometer (Horiba Jobin Yvon). The sample containing RBITC was diluted 4-fold prior to scanning. Absorbance scans were performed on a Spectra-Max 250 microplate reader, using 96-well quartz microplates (Molecular Devices, Sunnyvale, CA). For TEM imaging, CNC (0.1 mg/mL) was suspended in deionized water and sonicated to disperse the material. A well-dispersed suspension (8 $\mu$L) was then dried on a Formvar-carbon coated grid and analyzed. Low voltage transmission electron microscopy (LVTEM) micrographs were obtained by a Delong LVEM, low-voltage electron microscope (Soquelec, Montreal, QC, Canada) operating in TEM mode at 5 kV.

Confocal images were acquired using a 63×/1.4NA Plan Apochromat oil immersion DIC objective on a Zeiss LSM 5 Pascal confocal scan-head mounted on an Axiovert 200 M microscope stand. Confocal scanning was performed in multi-track mode using the following scan settings: 1024 × 1024 pixel format, zoom factor 2, voxel dimensions ($x$,$y$,$z$) = 0.07 $\mu$m × 0.07 $\mu$m × 0.8 $\mu$m, MBS = HFT 488/543/633, DBS1 = NFT545, pixel dwell time of 1.28 $\mu$s. Track-1 was configured to capture the FITC in Channel 2 using a 505−530 nm band-pass filter. The confocal pinhole aperture was set to 1.16 airy units (109 $\mu$m). The photomultiplier tube (PMT) gain setting was 830 V with an amplifier offset of 0.00 V. Track-2 was configured to capture RBITC in Channel 1 using a 560 nm long-pass filter. The PMT gain was 840 V with an offset of −0.13 V. No significant bleed-through was detected using these channel settings on single-stained control specimens. Z-stacks were acquired in 0.4 $\mu$m increments over a total distance of 10 $\mu$m for all 3-dimensional acquisitions except for R-293 image 2: R-293 z-stack1 (total sample thickness = 13.6 $\mu$m) and Mix-insect z-stack (total thickness = 26.4 $\mu$m).

The zeta potential ($\zeta$) of the nanomaterials (0.1% w/v) at different pHs was measured at 25 °C by a Zetasizer Nano ZS

(Malvern Instruments, Malvern, Worcestershire, UK) fitted with a high-concentration zeta potential cell (ZEN1010). In all measurements, 40 V were applied across an electrode spacing of 16 mm. The final value is an average of five repeated measurements for each sample.

**Cell Viability.** HEK-293 and *Sf*9 were cultivated in 125 mL sterile shake flasks (Corning, NY, USA) with a 20 mL working volume at a cell density of $1 \times 10^6$ cells/mL. The HyQ antibiotic/antimycotic 100X solution, 200 $\mu$L, (Thermo Scientific, Logan, UT, USA) was added to the cell culture to prevent bacterial or fungal contamination. CNC-RBITC (2 mL, 1 mg/mL) or CNC-FITC (2 mL, 1 mg/mL) was added to the cell cultures. Cell viability was assessed by the trypan blue exclusion assay during the course of experiments. In order to exclude any interaction between trypan blue and CNC that might alter the viability assay, *Sf*9 cells with different viabilities were nonspiked (negative control) or spiked with nonlabeled CNC. These effector cells were analyzed by the trypan blue exclusion assay. The *Sf9* cell viability was modified by putting the cells under mild or severe shear stress (vortexing) prior to the trypan blue assay. For the MTT cell viability assay, MTT dissolved in phosphate-buffered saline, pH 7.2, at 5 mg/mL was added to the *Sf9* cells (40 $\mu$L/well). After incubation at 27 °C for 2 h without (control) and in the presence of different concentrations of CNC-RBITC and CNC-FITC, cells were centrifuged at 350 g for 10 min and the medium aspirated. The formazan crystals were dissolved in 200 $\mu$L of dimethyl sulfoxide (DMSO) and the absorbance was measured at 570 nm in a micro plate reader. The viability of *Sf9* was calculated as cell viability (%) = average absorbance of wells/average absorbance of control wells.

**Electric Cell-Substrate Impedance Sensing (ECIS).** CNC was also assessed for its plausible cytotoxic or inhibitory effects using an ECIS system (Applied Biophysics, Troy, NY) with an insect cell model as previously reported (22). In brief, concanavalin A (Con A, 0.40 mL, 0.5 mg/mL, prepared fresh daily in 50 mM PBS, pH 7.4, with the aid of sonication for 1 h) was added into each of 8 wells of a sensing chip (8W1E, Applied Biophysics, Troy, NY) to coat the detecting gold electrodes (250 $\mu$m diameter). After protein adsorption (~30−60 min), the wells were washed 3 times with 0.85% NaCl and 0.4 mL of serum-free SF-900 II medium (Gibco BRL, Canadian Life Technologies, Burlington, ON, Canada) was placed in each well. The impedance baseline was monitored for 1−2 h at 27 °C in a humidified chamber. The wells were emptied before adding the insect cell suspension containing CNC. *Spodoptera frugiperda Sf*9 cells in serum-free SF-900 II medium were inoculated at an initial cell density of $0.4 \times 10^6$ cells/mL and grown to the midexponential phase of $2.5-3 \times 10^6$ cells/mL. The resulting cells were aseptically centrifuged at 1,500 rpm for 4 min and the pellets were thereafter suspended at a cell concentration of $3 \times 10^6$ cells/mL in a fresh medium. CNC (10 mg/mL stock) derived from pectate-lyase treated flax was added (2.5−50 $\mu$L) to 1.5 mL of the above cell suspension giving a concentration range of 17−333 $\mu$g/mL, before adding 0.4 mL of this mixture to 2 or 3 wells to test for possible cytotoxic/inhibitory effects. Five concentrations including a control were tested at the same time and the CNC sample was analyzed 3 different times. Similar experiments were conducted with CNC-FITC and CNC-RBITC. Detailed information of the experimental procedure and the estimation of the inhibition concentration ($ECIS_{50}$) can be found elsewhere (22, 23).

## RESULTS AND DISCUSSION

**Characterization of Cellulose Nanocrystal (CNC) and the CNC-RBITC Conjugate.** A CNC suspension was extracted from pectate lyase treated flax fibers by a modified acid hydrolysis method, which allowed for in situ purification and bleaching of the fibers during the preparation of CNC (5). The preparation produced individual and aggregated rod-like crystalline cellulose fragments, ranging from 10 to 20 nm in diameter with corresponding lengths of about 120−300 nm (Figure 1). FTIR spectra of the CNC showed absorption bands that were typical for cellulosic materials. The presence of signals at 1429, 1163, 1111, and 897 $cm^{-1}$ indicated that the CNC was primarily in the form of cellulose $I_\beta$ (30), i.e., there was no significant change of the conformation of the cellulose structure (see Figure S1 in the Supporting Information). For the observation of CNC by fluorescence spectroscopy, CNC was covalently conjugated with the RBITC fluorescent probe through an epoxy-mediated coupling reaction (Scheme 1). The resulting CNC-RBITC conjugate was thoroughly washed and dialyzed to remove unreacted dye, which might be adsorbed on the conjugate. Covalent conjugation between RBITC and CNC was confirmed by comparing CNC-RBITC against a blended mixture of CNC and RBITC on a thin layer chromatography plate (TLC). RBITC from the blended mixture behaved like the free dye and migrated on the TLC plate ($R_f = 0.78$, $CHCl_3$:$CH_3OH$ 9:1), whereas CNC-RBITC was retained at the base. Evidently, the organic phase could not wash away or dissociate RBITC when it was conjugated with CNC. Figure 2A shows the apparent color difference between the free RBITC (center) and the CNC-RBITC conjugates (right). The CNC-RBITC conjugate preserved the same rodlike shape of the pristine CNC with the dimensions of individual and aggregated rod-like crystalline cellulose fragments, with the same average dimensions (length and diameter) as pristine CNC (Figure 2B). The UV/vis spectra of the CNC-RBITC dispersion as well as the RBITC solution are shown in Figure 2C. For the former, the main 560-nm absorption band was attributed to the RBITC monomer, whereas the small 528 nm band, lying to the short-wavelength side of the monomer band,

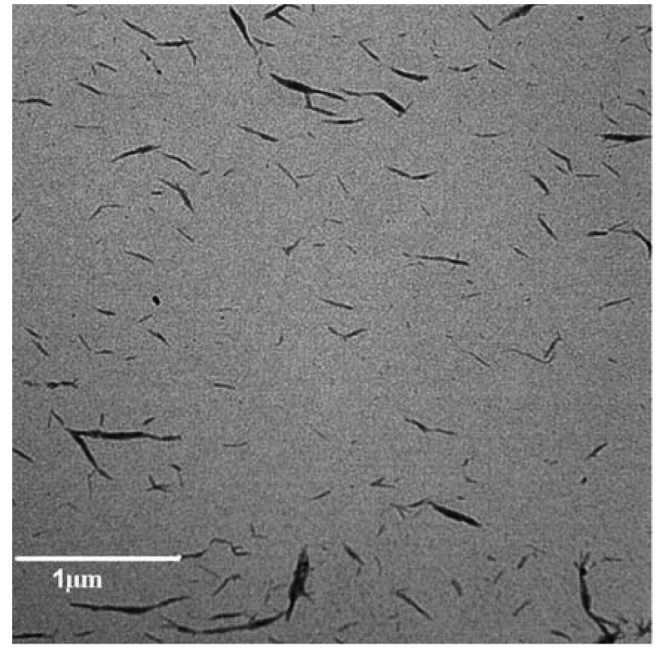


**FIGURE 1. TEM micrographs of pristine cellulose nanocrystals (CNC) show individual crystals with an average dimension of 10−20 nm wide and 120−300 nm long.**

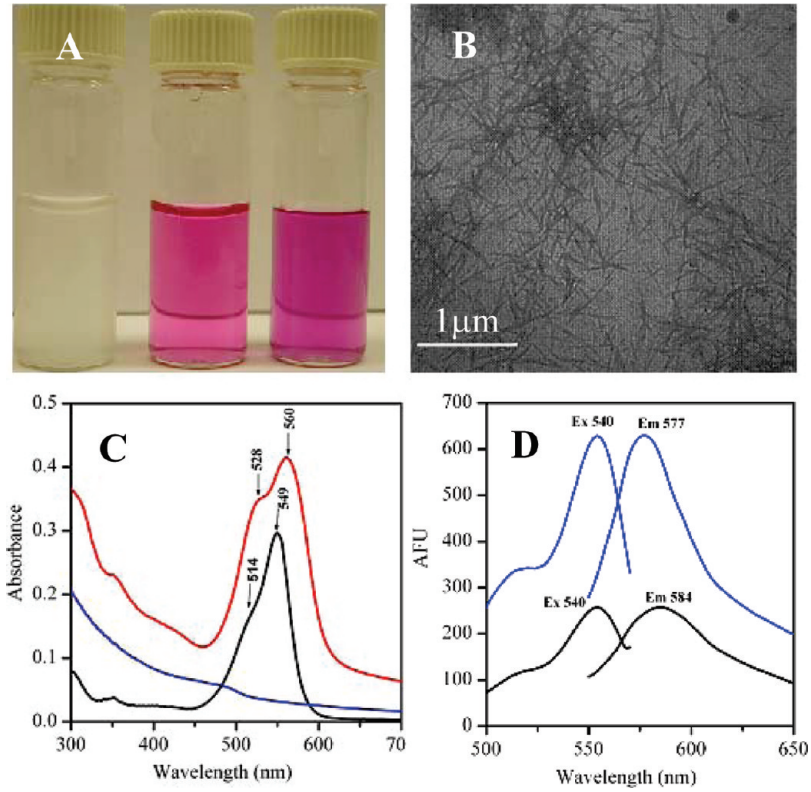


**FIGURE 2. (A) Photograph of an aqueous suspension of CNC, 1 wt % (left), free RBITC (center), and CNC-RBITC, 0.5 wt % (right). (B) TEM micrograph of CNC-RBITC. (C) UV/vis absorption spectra of an aqueous suspension of pristine CNC (blue), aqueous solution of RBITC (black), and an aqueous suspension of CNC-RBITC (red). (D) Fluorescent spectra of an aqueous solution of RBITC (blue) and an aqueous suspension of CNC-RBITC (black) (0.03 wt %, pH 6.4).**

was assigned to the aggregate absorption maximum. This was quite different from the absorption spectrum of the free RBITC solution with a maximal absorbance at 549 nm and a shoulder at 514 nm. With respect to fluorescence spectroscopy, both CNC-RBITC and free RBITC displayed the same excitation wavelength (540 nm). However, the fluorescence emission of CNC-RBITC occurred at 584 nm compared to 577 nm for the free RBITC aqueous solution (Figure 2D). The red shift and the significant decrease in fluorescence emission quantum yield as reflected by the absorption and fluorescence studies of RBITC could be attributed to the covalent attachment to CNC (31).

**Cellular Uptake Study.** Confocal microscopy was then used to investigate the cellular uptake of CNC-RBITC by HEK 293 and *Sf*9 cells (Figure 3). The cellular uptake of CNC-RBITC by HEK 293 cells (lower panel) and *Sf*9 cells (upper panel) was similar except for higher intensity in the second case. Such results indicated that CNC-RBITC was able to penetrate the cell membrane. The favorable electrostatic interaction between the cationic amino-terminated CNC-RBITC and the anionic cellular membrane could be the rationale behind such a high uptake (32). A video z-stacking imaging mode allows the visualization of the intracellular distribution of CNC-RBITC in the cell (Video 1). The distribution pattern revealed that CNC-RBITC was primarily dispersed through the cytoplasm, though some of CNC-RBITC was confined into the vesicular structure. No significant CNC-RBITC was present on the nucleus of both cell lines, indicating less interaction between these nanocrystals and the nuclear membrane. The fluorescence pattern observed for CNC-RBITC was unlikely related to the redistribution of free RBITC cleaved from the CNC conjugate since a different pattern was observed when the cells were incubated with free RBITC (data not shown). The morphological evidence shows some cells accumulated CNC-RBITC in endosomal/lysosomal compartments, favored by the cationic nature of the CNC-RBITC. Other studies suggest that cationic nanoparticles can penetrate the cellular membrane by making transient holes without causing substantial membrane disruption (33, 34).

Roman and co-workers have synthesized CNC-FITC and reported an insignificant uptake of this conjugate by human brain microvascular endothelial cells (HBMECs) (3, 27). To further address this issue in our study, we compared the cellular uptake capability of CNC-RBITC and CNC-FITC. A mixture of both conjugates (1 mg/mL each) was used in this competitive assay. Fluorescent and mixed-field confocal images showed that CNC-RBITC was capable of penetrating the cell membrane (Figure 4). In contrast, CNC-FITC formed aggregates only around the cells and could not permeate the cells. There was no significant uptake of the CNC-FITC bioconjugate by both cell lines at physiological pH. Such behavior could be the result of "repulsive forces" between the anionic hydroxyl-terminated CNC-FITC and the anionic cellular membrane, compared to more favorable electrostatic interaction between the cationic amino-terminated CNC-RBITC and the anionic cellular membrane. This was an important finding because the cellular uptake of CNC could

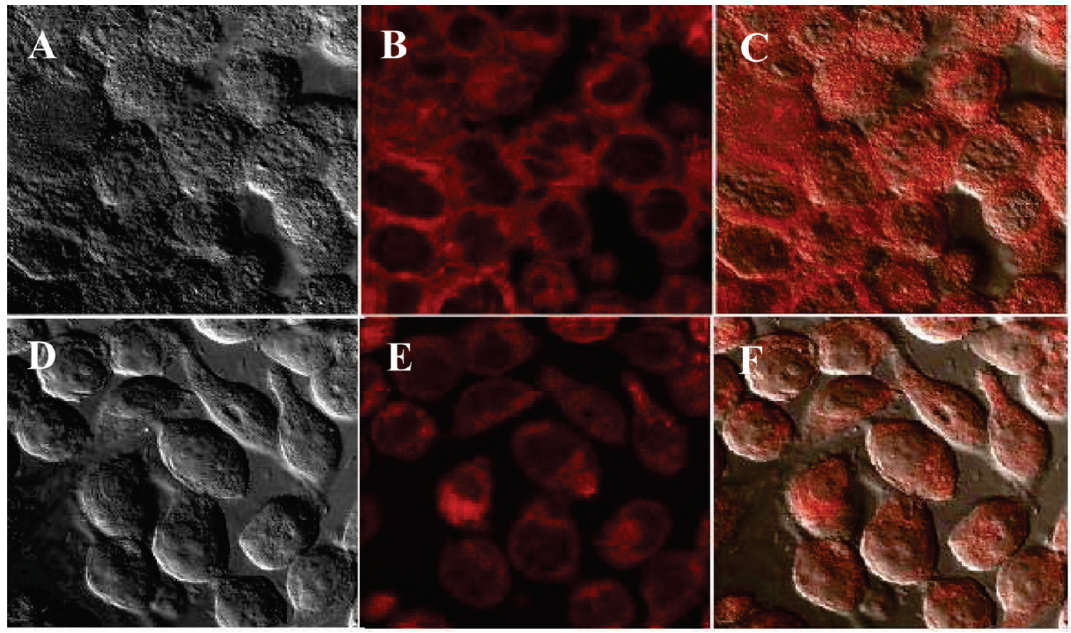


FIGURE 3. Confocal images of *Sf*9 cells treated with 0.1 mg/mL CNC-RBITC (upper panel) and HEK 293 cells treated with 0.1 mg/mL CNC-RBITC (lower panel): (A, D) bright field; (B, E) fluorescent field; (C, F) superimposed fields.

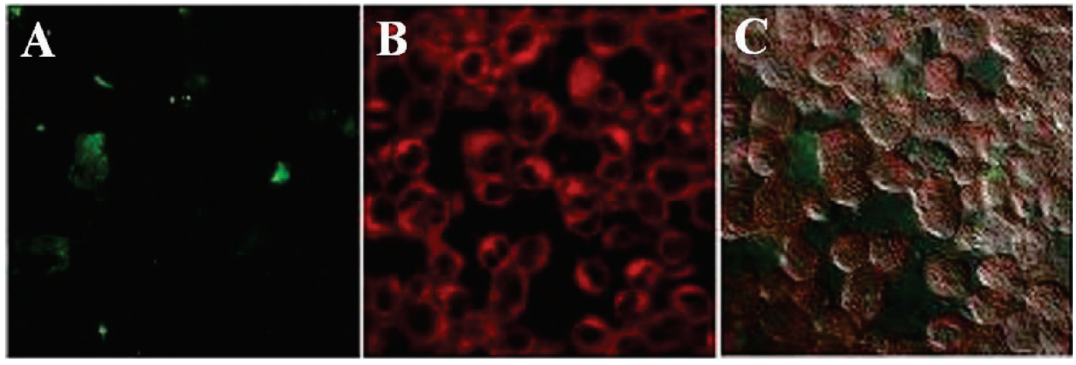


FIGURE 4. Confocal images of *Sf*9 cells incubated with a mixture of 0.1 mg/mL CNC-RBITC and 0.1 mg/mL CNC-FITC. (A) FITC fluorescence field, (B) RBITC fluorescence field, and (C) both FITC and RBITC fluorescence fields.

be readily controlled by fine-tuning the surface functionality of CNC. The dimensions and the aggregation pattern of CNC did not change after modification with both FITC and RBITC as attested by TEM imaging (see Figure S2 in the Supporting Information). In addition, the label loading was similar in both cases: 0.033 mmol/g CNC and 0.032 mmol/g CNC for FITC and RBITC, respectively (27).

**pH Effect.** The pH effect on the cellular uptake of the two fluorescent nanofibers in the growth medium was then examined during the course of incubation. The surface modification of CNC with different charged groups resulted in different $\zeta$ potentials. The overall surface charge of the nanoparticles was dependent on the functional group present on their surface, being positive for CNC-RBITC ($\zeta = 8.7$ mV) and negative for CNC-FITC ($\zeta = -46.4$ mV). The average $\zeta$-potential of pristine CNC was $-31.3$ mV. Generally, for surface modified nanoparticles, the dissociation of an acidic group, e.g., a carboxylic acid moiety, results in a negatively charged surface, whereas the dissociation of a basic group on a nanoparticle surface will yield a positively charged surface (35). Altering the medium pH will alter the surface charge of nanoparticles, which in turn affects the binding between nanoparticles and cellular substituents, and eventually the cell internalization mechanisms (36, 37). This altered charge distribution of the nanoparticles could be beneficial for drug/fluorescent probe carrier systems, because the charge-tunable nanoparticles might enhance the accumulation efficiency in the target cells (38).

The cellular uptake of negatively charged CNC-FITC displayed strong pH-dependency (Figure 5A, B). At physiological and basic pH (6.5 and 8.0), the total uptake by *Sf*9 and HEK 293 was insignificant; however, at pH $\sim$ 5, the fibers were presumably in the protonated form and became membrane permeable. For CNC-RBITC, the particles were insensitive to pH, which facilitated the total internalization at the three examined pHs. The internalization rate as reflected by fluorescence intensity increased exponentially and approached a plateau after 3 h into the experiment (Figure 5C,D). The fluorescence intensity inside the cell was slightly higher at pH 5 with CNC-RBITC, demonstrating that positively charged nanoparticles were endocytosed faster than neutral or negative nanoparticles (39). Notice that both cell lines tended to aggregate at pH $\sim$8 and the fluorescence intensity started decreasing after 5 h. To correlate this strong

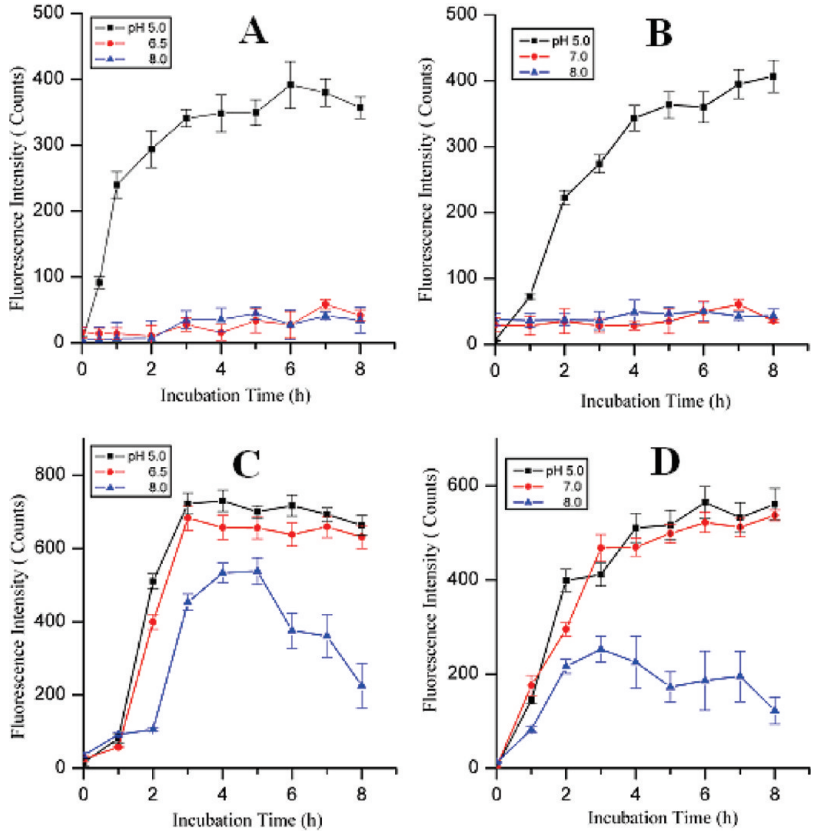


**FIGURE 5. Effect of incubation time on CNC-FITC (0.1 mg/mL) with (A) *Sf*9 cells and (B) HEK-293 cells and CNC-RBITC (0.1 mg/mL) with (C) *Sf*9 cells and (D) HEK-293 cells at different extracellular pHs. Cells were incubated with the nanofibers in growth medium at pH 5.0, 6.5 (*Sf*9 cells), 7.0 (HEK-293 cells), and 8.0 for a total time of 8 h. The fluorescence was measured in the lysate of the cells using a 96-well microplate reader. Each data point represents the average ± standard error of three experiments (cell density of 1 × $10^6$ cells/mL).**

**Table 1. ζ-Potential As a Function of pH for CNC-FITC and CNC-RBITC (0.1% w/v) at 25°C ($n = 5, \pm 0.05$)**

| | ζ-potential (mV) | |
|---|---|---|
| pH | CNC-FITC | CNC-RBITC |
| 5.0 | −3.9 | 9.0 |
| 7.0 | −46.4 | 8.7 |
| 8.0 | −48.7 | 8.6 |

pH effect with the surface charge of the nanomaterials, the ζ-potential was measured for both CNC-FITC and CNC-RBITC at the three pHs tested in this study. The results indicated that, while no significant change was observed for CNC-RBITC, the pH exhibited a pronounced effect on the ζ-potential of CNC-FITC at pH 5 ($\zeta = -3.9$ mV) compared to ($\zeta = -46.4, -48.7$ mV) at pH 7 and 8, respectively (Table 1).

Confocal fluorescence microscopy was used to confirm the dissimilar responses of the two modified CNC nanoparticles to pH variation. Figure 5 compares the internalization pattern of CNC-FITC (upper) and CNC-RBITC (lower) by the *Sf*9 cell line at two different pHs. At pH 5, both nanoparticles (CNC-FITC and CNC-RBITC) were able to permeate the cell membrane (Figure 6A). However, at pH 6.5, only CNC-RBITC was internalized by cells, meanwhile CNC-FITC did not show any significant presence inside the cells (Figure 6B). Although both CNC-FITC and CNC-RBITC were internalized by *Sf*9 cells at pH 5, this pH was not suitable for cell growth as the cell viability was adversely affected after long incubation periods regardless of which nanoparticles were assessed. Literature studies indicate that surface charge characteristics may determine the fate of nanoparticles in cells. Surface functionalization of gold nanoparticles with PEG results in efficient internalization in endosomes and cytosol, and localization in the nuclear region (40). Poly(DL-lactide-co-glycolide) nanoparticles are known to be ingested by cells by endocytosis (41, 42). A change in surface charge from negative to positive of the PLGA nanoparticles results in cytoplasmic delivery of the incorporated drugs. Apparently, the positive surface charge provokes the escape of the endosomes into the cellular cytoplasm. In contrast, negatively charged polystyrene nanoparticles remain in the endosomal compartment of the smooth muscle cells, i.e., they do not reach the cytosol (41).

**Aggregation and Cell Viability.** The aggregation pattern and the cell viability test were performed and the results indicated a nontoxic effect of CNC-RBITC on the two cell lines. The addition of CNC-RBITC to the cell cultures triggered cellular aggregation and this behavior was observed in both cell lines, being more evident in *Sf*9 cells. HEK-293 cells aggregated in small clusters having only a few cells (Figure 7B), whereas *Sf*9 cells showed more tendency to aggregate forming massive cellular clusters, and scarce "free cells" (Figure 7D). No aggregation was observed when CNC-RBITC was not added to the cell cultures (Figure 7A,C). On the basis of these results, a cell viability test was

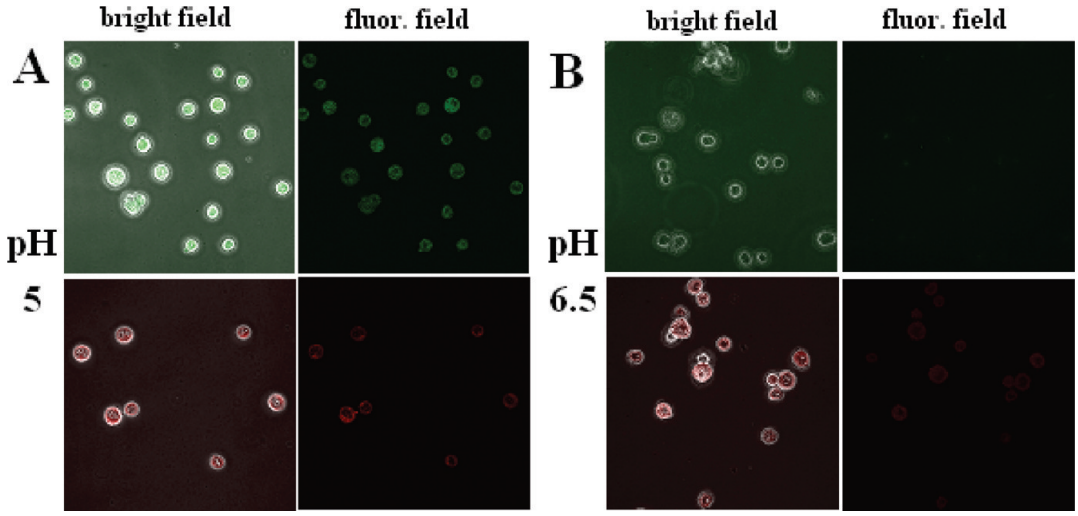


FIGURE 6. Mixed field and fluorescence-microscopy images comparing the uptake of CNC-FITC (upper) with CNC-RBITC (lower) by *Sf*9 cells at (A) pH 5 and (B) pH 6.5. Cells were incubated with CNC-FITC or CNC-RBITC during 3 h at respective pH, and then fixed for confocal microscope measurement.

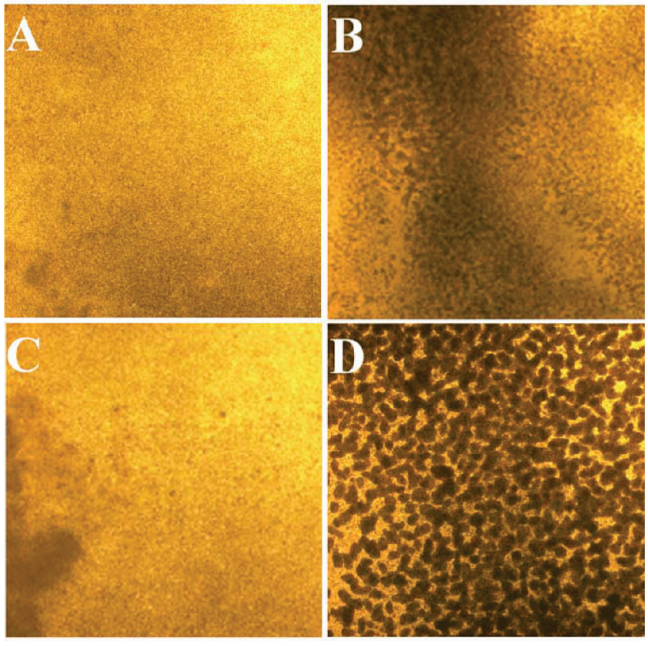


FIGURE 7. Cellular aggregation by the addition of CNC-RBITC (0.1 mg/mL). (A) HEK-293 cells control cultures (no CNC-RBITC). (B) HEK-293 cells 24 h after CNC-RBITC addition. (C) *Sf*9 cells control cultures (no CNC-RBITC). (D) *Sf*9 cells 24 h after CNC-RBITC addition.

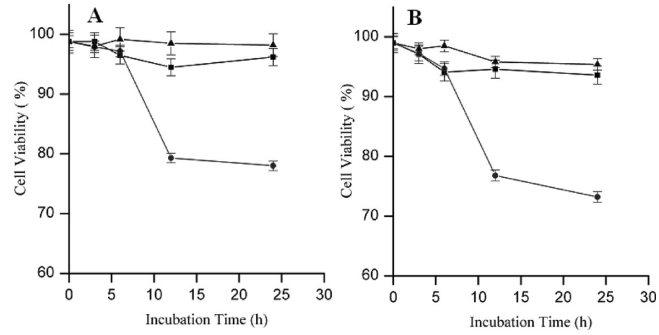


FIGURE 8. (A) A trypan blue *Sf*9 and (B) HEK-293 cell viability profiles of control (▲), and after addition of CNC-RBITC (□) or CNC-FITC (•) (0.1 mg/mL). Each data point represents the average ± SE of three viability measurements (cell density of $1 \times 10^6$ cells/mL).

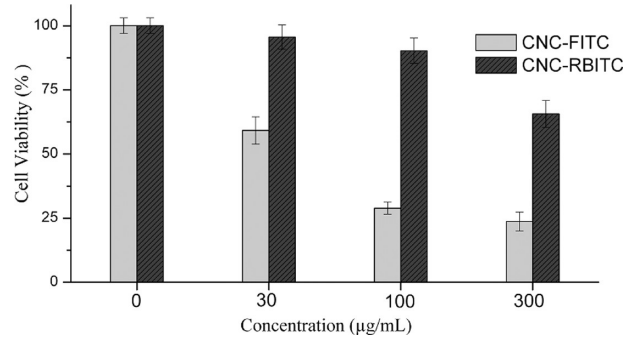


FIGURE 9. MTT cell viability profile of *Sf*9 after exposure to different concentrations of CNC-FITC and CNC-RBITC. Each data point represents the average ± SE of three viability measurements (cell density of $1 \times 10^6$ cells/mL).

performed through the time-course of the cellular uptake study to assess whether CNC-RBITC or CNC-FITC might have an impact on the cell membrane integrity and therefore the cell viability. The trypan blue exclusion assay confirmed that HEK-293 viability did not decrease 24 h after the CNC-RBITC addition, i.e., these nanocrystals exhibited no impact in either cell viability or the membrane integrity (Figure 8). Similar results were observed for *Sf*9 cells, indicating no cytotoxic effects of the CNC-RBITC during the time-course of the cellular uptake study. In contrast, CNC-FITC exhibited cytotoxic effects almost immediately after incubation and the cell viability started decreasing dramatically after 5 h in both cell lines. HEK-293 was slightly more affected (71 % of viability) than *Sf*9 cells (77 % of viability). The assay was not interrupted by a possible adsorption of the trypan blue dye on CNC since there was no significant difference in viability between *Sf*9 cells both spiked and nonspiked with unlabeled CNC (see Figure S3 in the Supporting Information).

The MTT assay was also performed to further support our results. The cell viability profile of *Sf*9 as a response to increasing concentrations of CNC-FITC and CNC-RBITC after 24 h exposure is shown in Figure 9. Similar to the trypan blue assay, at 30 $\mu$g/mL CNC-RBITC, the cell viability did not significantly change compared to the control (within the

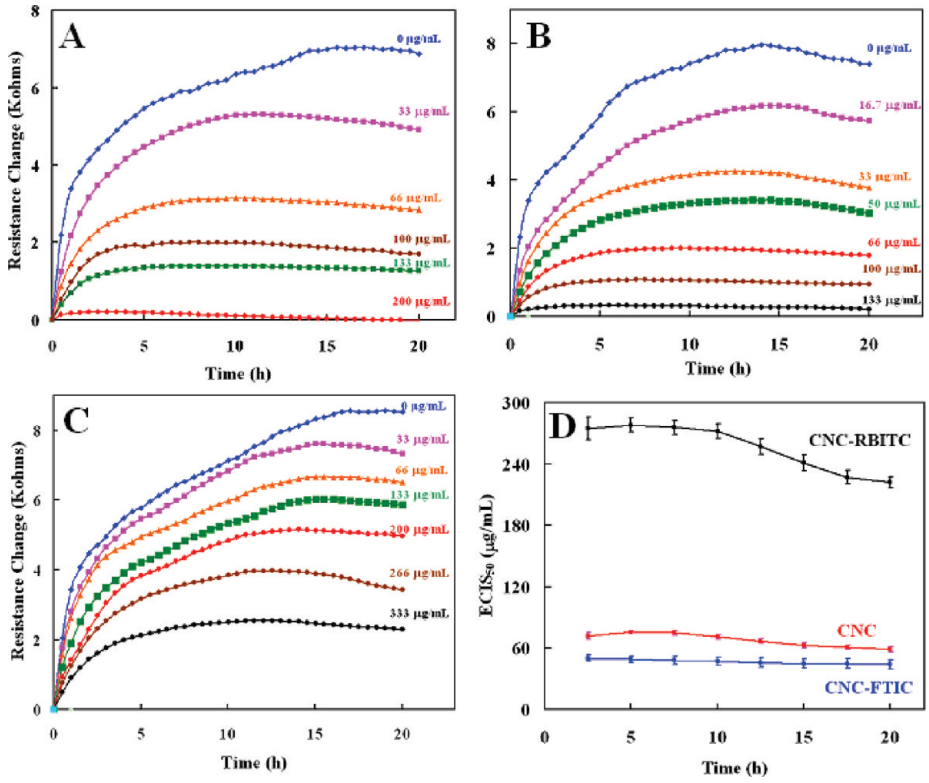


**FIGURE 10. Resistance response change (ΔkΩ) of *Sf*9 cells to different concentrations of (A) CNC, (B) CNC-FITC, and (C) CNC-RBITC. (D) The $ECIS_{50}$ value ($n = 3$, ± SEM) obtained for the three conjugates was derived from data sets (A, B, and C) by using the time response function $f(C, t)$ to construct a series of inhibition curves at any given time $t_0$ (>2.5 h) for different CNC concentrations (16.7−333 μg/mL).**

experimental error margins). At 100 μg/mL CNC-RBITC, the cell viability slightly decreased to 90%. However, CNC-FITC displayed an immediate impact on the cells and the viability was 59% at 30 μg/mL and 32% at100 μg/mL. At higher concentrations (300 μg/mL) the cell viability was 29% for CNC-FITC compared to 66% for CNC-RBITC. These results confirmed the non toxicity of CNC-RBITC compared to CNC-FITC at concentrations below 100 μg/mL.

**Probing Cytotoxicity Effect by ECIS.** A series of experiments was carried out with ECIS to quantify any plausible effect of CNC-FITC, CNC-RBITC, as well as the pristine CNC. The attachment and spreading of *Sf*9 cells attached to the surface of a gold electrode precoated with Con A would be affected by the presence of toxic/inhibitory compounds, resulting in a disruption of the current flow at the substratum level. The *Sf*9 cell suspension was mixed with CNC-FITC, CNC-RBITC, or CNC at different concentrations and allowed to spread on Con A-coated gold surfaces. As expected, the inhibitory effect was concentration dependent for all three conjugates tested. There was no significant effect up to 5 μg/mL CNC; however, at 33 μg/mL, inhibition was easily observed and the effect was amplified as the concentration increased to 200 μg/mL (Figure 10A). Within the first few hours, the resistance profiles were already different from the control (without CNC). It was likely that after the initial adherence of the cells CNC interfered with the cell spreading as the cells were not as well spread on the electrode surface, which could result from the negative charge present on the CNC surface. The inhibitory effect could occur at the level of the extracellular matrix (ECM) or protein coating. At 200 μg/mL, the cells were spherical compared to the well spread *Sf*9 cells observed in the absence of the CNC. Similar inhibitory effects have been reported for *Antrodia camphorata* isolates and destruxins from *Metarhizium anisopliae* (23, 24). CNC-FITC showed a comparable pattern to pristine CNC and the inhibitory effect was observed immediately after incubation (16.7 μg/mL) as shown in Figure 10B. At the highest concentration (133 μg/mL), the cells on the electrode surface were spherical compared to the wells without CNC-FITC. In the presence of CNC-RBITC (Figure 10C), the inhibitory effect was much less pronounced compared to CNC or CNC-FITC as inhibition was only apparent between 30−50 μg/mL. At very high concentrations of CNC-RBITC (>333 μg/mL) the shape of the cells was spherical. Thus, the positive charge related to the CNC-RBITC displayed a less detrimental effect on the cell spreading on the gold surface.

The half-inhibition concentration ($ECIS_{50}$) for the three cases was calculated from the data obtained in Figures 10A−C. The time response function $f(C, t)$ was used to construct a series of inhibition curves at any given time $t_0$ (>2.5 h) for different CNC concentrations (16.7−333 μg/mL) used (23). The normalized time response function decreased as expected as the concentration of CNC (≥16.7 μg/mL) increased for all exposure times considered (figure not shown). Figure 10D shows the relationship between the half-inhibition concentration and exposure time, with the average and standard error on the mean (SEM) given for three runs. The enhanced inhibition of either CNC or CNC-FITC on the cells compared to CNC-RBITC could be easily observed from the measurements of $ECIS_{50}$ immediately after

*Sf*9 cell addition. Although the effect could be seen immediately, $ECIS_{50}$ values were calculated starting at 2.5 h. $ECIS_{50}$ values slowly decreased and reached a plateau after 15−20 h. The resulting $ECIS_{50}$ values were 61 ± 2.4, 45 ± 4.6, and 224 ± 6.3 $\mu$g/mL for CNC, CNC-FITC, and CNC-RBITC, respectively. In comparison to CNC-FITC, the inhibition due to CNC-RBITC on *Sf*9 cells was significantly lower, in agreement with that of the cell viability and confocal imaging assays.

## CONCLUSIONS

In brief, we have demonstrated the ability of functionalized CNC to penetrate cells, with no indication of cytotoxicity. CNC could be considered as a new generation of drug nanocarriers or bioimaging probes considering its high surface area of 150 $m^2$/g (43). The surface charge of CNC could be tuned for penetration inside the cell without causing cellular damage. CNC-RBITC was uptaken by HEK 293 and *Sf*9 cells without affecting the cell membrane integrity, whereas no significant internalization of CNC-FITC was noted at physiological pH. CNC-RBITC exhibited no noticeable cytotoxicity at the studied concentrations on the two cell lines under investigation. As a natural material with good tolerance by the body, cellulose has been routinely used in medical and pharmaceutical applications. CNCs possess reactive functional groups on their surface to which drugs, nanoparticles, or targeting molecules could be attached. Such features, together with noncytotoxicity and membrane permeability, make them perfect candidates for development of a new generation of optical bioimaging and drug delivery systems.

**Acknowledgment.** This research was supported by the Canada National Bioproducts Program. We are grateful to the Imaging facility (McGill University Life Sciences Complex), Montreal, Canada, for performing confocal microscopy. Thanks are extended to Antoine Caron and Paule Lachance, Biotechnology Research Institute, Montreal, Canada, for the fluorescence spectroscopy measurement.

**Supporting Information Available:** Additional figures (PDF); video (AVI). This material is available free of charge via the Internet at http://pubs.acs.org.

### REFERENCES AND NOTES

(1) Samir, M. A. S. A.; Alloin, F.; Sanchez, J.-Y.; El Kissi, N.; Dufresne, A. *Macromolecules* **2004**, *37*, 1386–1393.
(2) Fleming, K.; Gray, D. G.; Matthews, S. *Chem.—Eur. J.* **2001**, *7*, 1831–1835.
(3) Roman, M.; Dong, S.; Hirani, A.; Lee, Y. W. In *Polysaccharide Materials: Performance by Design*; American Chemical Society: Washington, D.C., 2009; pp 81−91.
(4) Habibi, Y.; Lucia, L. A.; Rojas, O. J. *Chem. Rev.* **2010**, *110*, 3479–3500.
(5) Mahmoud, K. A.; Male, K. B.; Hrapovic, S.; Luong, J. H. T. *ACS Appl. Mater. Interfaces* **2009**, *1*, 1383–1386.
(6) Alberts, B.; Johnson, A.; Lewis, J.; Raff, M.; Roberts, K.; Walter, P. *Molecular Biology of the Cell*, 4th ed.; Garland Science: New York, 2002.
(7) Vallet-Regi, M.; Balas, F.; Arcos, D. *Angew. Chem., Int. Ed.* **2007**, *46*, 7548–7558.
(8) Slowing, I. I.; Trewyn, B. G.; Giri, S.; Lin, V. S. Y. *Adv. Funct. Mater.* **2007**, *17*, 1225–1236.
(9) Schlossbauer, A.; Schaffert, D.; Kecht, J.; Wagner, E.; Bein, T. *J. Am. Chem. Soc.* **2008**, *130*, 12558–12559.
(10) Hong, R.; Han, G.; Fernandez, J. M.; Kim, B.; Forbes, N. S.; Rotello, V. M. *J. Am. Chem. Soc.* **2006**, *128*, 1078–1079.
(11) Lee, J.-H.; Lee, K.; Moon, S. H.; Lee, Y.; Park, T. G.; Cheon, J. *Angew. Chem., Int. Ed.* **2009**, *48*, 4174–4179.
(12) Nam, J.; Won, N.; Jin, H.; Chung, H.; Kim, S. *J. Am. Chem. Soc.* **2009**, *131*, 13639–13645.
(13) Jin, Y.; Gao, X. *J. Am. Chem. Soc.* **2009**, *131*, 17774–17776.
(14) Son, S. J.; Reichel, J.; He, B.; Schuchman, M.; Lee, S. B. *J. Am. Chem. Soc.* **2005**, *127*, 7316–7317.
(15) Dubertret, B.; Skourides, P.; Norris, D. J.; Noireaux, V.; Brivanlou, A. H.; Libchaber, A. *Science* **2002**, *298*, 1759–1762.
(16) Gao, Z.; Lukyanov, A. N.; Singhal, A.; Torchilin, V. P. *Nano Lett.* **2002**, *2*, 979–982.
(17) Torchilin, V. P.; Lukyanov, A. N.; Gao, Z. *Proc. Natl. Acad. Sci. U.S.A.* **2003**, *100*, 6039–6044.
(18) Park, J.-H.; van Maltzahn, G.; Ruoslahti, E.; Bhatia, S. N.; Sailor, M. J. *Angew. Chem., Int. Ed.* **2008**, *47*, 7284–7288.
(19) Youssef Habibi, Y.; Lucia, L. A.; Rojas, O. J. *Chem. Rev.* **2010**, *110*, 3479–3500.
(20) Owens, D. E., 3rd; Pappar, N. A. *Int. J. Pharm.* **2006**, *307*, 93–102.
(21) Zheng, L.-Y.; Zhu, J.-F. *Carbohydr. Polym.* **2003**, *54*, 527–530.
(22) Luong, J. H. T.; Habibi-Razaei, M.; Meghrous, J.; Xiao, C.; Male, K. B.; Kamen, A. *Anal. Chem.* **2001**, *73*, 1844–1848.
(23) Xiao, C.; Lachance, B.; Sunahara, G.; Luong, J. H. T. *Anal. Chem.* **2002**, *74*, 5748–5753.
(24) Male, K. B.; Lachance, B.; Hrapovic, S.; Sunahara, G.; Luong, J. H. T. *Anal. Chem.* **2008**, *80*, 5487–5493.
(25) Male, K. B.; Rao, Y. K.; Tzeng, Y.-M.; Montes, J.; Kamen, A.; Luong, J. H. T. *Chem. Res. Toxicol.* **2008**, *21*, 2127–2133.
(26) Male, K. B.; Tzeng, Y.-M.; Montes, J.; Liu, B.-L.; Liao, W.-C.; Kamen, A.; Luong, J. H. T. *Analyst* **2009**, *134*, 1447–1452.
(27) Dong, S.; Roman, M. *J. Am. Chem. Soc.* **2007**, *129*, 13810–13811.
(28) Porath, J.; Fornstedt, N. *J. Chromatogr.* **1970**, *51*, 479–489.
(29) Swoboda, G.; Hasselbach, W. Z. *Z. Naturforsch: Biosci.* **1985**, *40*, 863–875.
(30) Higgins, H. G.; Stewart, C. M.; Harrington, J. K. *J. Polym. Sci.* **1961**, *51*, 59–84.
(31) Vieira Ferreira, L. F.; Cabral, P. V.; Almeida, P.; Oliveira, A. S.; Reis, M. J. *Macromolecules* **1998**, *31*, 3936–3944.
(32) Kumar, R.; Roy, I.; Ohulchanskyy, T. Y.; Goswami, L. N.; Bonoiu, A. C.; Bergey, E. J.; Tramposch, K. M.; Maitra, A.; Prasad, P. N. *ACS Nano* **2008**, *2*, 449–456.
(33) Leroueil, P. R.; Hong, S.; Mecke, A.; Baker, J. R.; Orr, B. G.; Banaszak-Holl, M. M. *Acc. Chem. Res.* **2007**, *40*, 335–342.
(34) Zhang, Z.-Y.; Smith, B. D. *Bioconjugate Chem.* **2000**, *11*, 805–814.
(35) Berga, J. M.; Romosera, A.; Banerjeea, N.; Zebdaa, R.; Sayesa, C. M. *Nanotoxicology* **2009**, *3*, 276–283.
(36) Lundqvist, M.; Stigler, J.; Giuliano, E.; Lynch, I.; Cedervall, T.; Dawson, K. *Proc. Natl. Acad. Sci. U.S.A.* **2009**, *105*, 14265–14270.
(37) Al-Jamal, W. T.; Al-Jamal, K. T.; Bomans, P. H.; Frederik, P. M.; Kostarelos, K. *Small* **2008**, *4*, 1406–1435.
(38) Kim, W. J.; Bonoiu, A. C.; Hayakawa, T.; Xia, C.; Kakimoto, M.-a.; Pudavar, H. E.; Lee, K.-S.; Prasad, P. N. *Int. J. Pharm.* **2009**, *376*, 141–152.
(39) Murphy, R. F.; Powers, S.; Cantor, C. R. *J. Cell Biol.* **1984**, *98*, 1757–1762.
(40) Shenoy, D.; Fu, W.; Li, J.; Crasto, C.; Jones, G.; DiMarzio, C.; Sridhar, S.; Amiji, M. *Int. J. Nanomed.* **2006**, *1*, 51–57.
(41) Panyam, J.; Zhou, W.-Z.; Prabha, S.; Sahoo, S. K.; Labhasetwar, V. *FASEB J.* **2002**, *16*, 1217–1226.
(42) Konan, Y. N.; Chevallier, J.; Gurny, R.; Allemann, E. *Photochem. Photobiol.* **2003**, *77*, 638–644.
(43) Terech, P.; Chazeau, L.; Cavaille, J. Y. *Macromolecules* **1999**, *32*, 1872–1875.

AM1006222